

## Modeling circulation in lakes: Spatial and temporal variations

*Bernard Laval*<sup>1</sup> and *Jörg Imberger*

Department of Environmental Engineering, Centre for Water Research, University of Western Australia, Crawley, 6009, Western Australia, Australia

*Ben R. Hodges*

Department of Civil Engineering, Mail Code C1786, University of Texas at Austin, Austin, Texas 78712-1076

*Roman Stocker*<sup>2</sup>

Department of Environmental Engineering, Centre for Water Research, University of Western Australia, Crawley, 6009, Western Australia, Australia

### *Abstract*

The influence of spatial and temporal variations in wind forcing on the circulation in lakes is investigated using field data and the three-dimensional Estuary and Lake Computer Model (ELCOM) applied to Lake Kinneret. Lake Kinneret field data from six thermistor chains and eight wind anemometers deployed during July 2001 are presented. Internal wave motions are well reproduced by the numerical model when forced with a spatially uniform wind taken from a station near the lake center; however, simulated seiche amplitudes are too large (especially vertical mode 2) and lead observations by 3–10 h (for a 24-h period wave) at different locations around the lake. Consideration of the spatial variation of the wind field improves simulated wave amplitude, and phase error at all stations is reduced to less than 1.5 h. This improvement is attributable to a better representation of the horizontally averaged wind stress and can be reproduced with a spatially uniform wind that has the same horizontally averaged wind stress as the spatially varying wind field. However, a spatially varying wind field is essential for simulating mean surface circulation, which is shown to be predominantly directly forced by the surface-layer-averaged wind stress moment.

Wind blowing over a lake surface forms a highly turbulent surface mixing layer. Turbulence rapidly distributes momentum, transferred from wind to water, over the depth of this layer such that (initially) the surface water moves downwind as a slab (Spigel and Imberger 1980). Basin-scale, wind-induced motions depend on interactions of spatially and temporally varying wind forcing with bathymetry, density distribution, and the earth's rotation. These motions include basin-scale internal waves driven by temporal variations in

wind stress and basin-scale mean circulation driven by spatial variations in wind stress (direct circulation) or by rectification of internal wave motions (residual circulation) (Strub and Powell 1986). Energy from basin-scale motions is dissipated via turbulent mixing at the lake boundary or by shear in the lake interior when there is density stratification (see Imberger [1998] for a review).

During summer months, Lake Kinneret in Israel is highly temperature stratified and strongly forced by a daily sea breeze. The resulting basin-scale internal seiches are dominated by a vertical mode 1, 24-h-period Kelvin wave, accompanied by 12- and 20-h Poincaré waves in both vertical modes 1 and 2 (Antenucci et al. 2000). Using analytic and numerical methods, Ou and Bennett (1979) showed that the mean cyclonic surface-layer circulation could be explained using a spatially uniform wind and, hence, could be classified as residual circulation. More recently, Pan et al. (2002) used the surface wind field predicted by a three-dimensional (3D) atmospheric model to force a 3D hydrodynamic model of Lake Kinneret. They showed that the curl of the wind stress could account for the simulated depth-averaged vorticity and, hence, that the mean circulation in Lake Kinneret is direct. Numerical model results presented in this article confirm the interpretation of Pan et al. (2002).

This work considers the effects of spatial and temporal variability in the wind field on basin-scale motions in lakes. We begin with a description of the numerical methods used to reproduce the internal wave field in Lake Kinneret. We then show that the next model skill level for representing evolution of the dynamic density field in a lake requires both

<sup>1</sup> To whom correspondence should be addressed. Present address: Department of Civil Engineering, University of British Columbia, Vancouver, BC, V6T 1Z4, Canada (blaval@civil.ubc.ca).

<sup>2</sup> Present address: Department of Applied Mathematics, MIT, 2-339, 77, Massachusetts Ave., Cambridge, Massachusetts 02139 (stocker@math.mit.edu).

### *Acknowledgments*

The first author was the recipient of an international postgraduate research scholarship and a University of Western Australia postgraduate award. The field experiments were funded by the Israeli Water Commission, via the Kinneret modeling project, conducted jointly by the Kinneret Limnological Laboratory and the Centre for Water Research. The support of the Kinneret Limnological Laboratory and Centre for Water Research field staff is gratefully acknowledged. The authors thank Jason Antenucci and Robert Spigel for comment on an earlier version of this manuscript. Ben R. Hodges was partially supported by an Office of Naval Research Young Investigator Program Award, grant N00014-01-1-0574, Program Officer Manuel Fiadeiro. Roman Stocker was the recipient of G. Marin and A. Gini scholarships. This article represents Centre for Water Research reference ED 1693-BL.

spatial and temporal wind variability in the model boundary conditions. Finally, we describe the effects of a spatially varying wind field on the surface circulation by considering the surface-layer-averaged vorticity balance.

### Numerical method

*Estuary and Lake Computer Model*—The Estuary and Lake Computer Model (ELCOM) solves the 3D, hydrostatic, Boussinesq, Reynolds-averaged Navier Stokes and scalar transport equations separating mixing of scalars and momentum from advection (Hodges 2000; Hodges et al. 2000). Free-surface evolution is modeled using the semi-implicit method of Casulli and Cattani (1994). Momentum advection uses an Euler–Lagrange scheme (Staniforth and Côté 1991; Casulli and Cheng 1992), whereas scalar transport is by the conservative, flux-limiting, explicit differentiation scheme, ULTIMATE-QUICKEST (Leonard 1991). Simulations were started from rest, with horizontal free surface and isopycnals. No-slip boundary conditions were used for bottom boundaries, and free-slip boundary conditions were used for side land-boundaries. Wind stress at the surface boundary is modeled as a momentum source distributed evenly over the surface wind-mixed layer (see “mixing-layer model”). Wind stress is calculated from wind velocity using a bulk formulation:

$$\tau_w = \rho_a C_D |\mathbf{u}_w| \mathbf{u}_w \quad (1)$$

where  $\rho_a$  is the density of air taken as  $1.2 \text{ kg m}^{-3}$ ,  $C_D$  is a coefficient of drag, and  $\mathbf{u}_w$  is the wind velocity measured 10 m above the water surface.

The first-order effect of numerical diffusion in simulations dominated by large internal wave motions (i.e., large isopycnal displacements relative to a fixed numerical grid) is a spurious thickening of the metalimnion, quantified by change in background potential energy occurring during the advection of mass. The cumulative effects of numerical diffusion can be controlled by the filtering technique of Laval et al. (2003), which was used in all present Kinneret simulations.

ELCOM uses an Arakawa C-grid (velocities defined on cell faces with free-surface height and scalar concentrations defined on cell centers). As scalars and momentum are mixed based on velocity shear and density gradients, the vertical mixing algorithm requires some form of interpolation to collocate density, velocity, and mixing. Hodges et al. (2000) linearly interpolated horizontal velocity components to cell centers to compute shear production and momentum mixing and then interpolated the resulting velocity field back to the cell faces. This approach is effectively a  $2\Delta x$  smoothing operation, which smoothed sharp horizontal gradients of velocity across the sloping metalimnion in simulations of Lake Kinneret. Smoothing of horizontal velocity gradients reduces the advective kinetic energy of the internal wave motions, resulting in the damping of internal waves. This damping was discussed in Hodges et al. (2000), but the source was incorrectly hypothesized to be boundary condition effects. In the present work, we retain (1) collocation of velocity for purposes of computing the velocity shear turbulent kinetic energy source term and (2) mixing computa-

tion of scalars and momentum at the cell centers. However, instead of interpolating the mixed velocity field back to the cell faces, we linearly interpolate the velocity change caused by the mixing (see Dietrich 1997). This approach reduced the observed damping of seiche motions in test simulations of Lake Kinneret (not shown).

*Mixing-layer model*—The mixing model developed here is based on the one-dimensional integral mixing model of Spigel et al. (1986), adapted by way of Hodges et al. (2000) to 3D fixed-grid architecture. Mixing is computed separately in each water column, starting from the free surface and operating downward through grid layers. Homogenization of properties between two layers occurs wherever the calculated turbulent kinetic energy available for mixing ( $E_A$ ) is larger than the potential energy required for mixing ( $E_R$ ) and the dissipation encountered during mixing. Since the horizontal cross-sectional area of each water column does not vary with depth, all energies are computed on a per-unit area basis.  $E_A$  is parameterized as the sum of energy available for mixing because of wind stirring and internal shear. The component of  $E_A$  attributed to wind stirring is assumed to be proportional to  $u_*^3 \Delta t$  (Kraus and Turner 1967), where  $\Delta t$  is the computation time step and  $u_*^2 = \rho_o^{-1} |\tau_w|$  is the wind shear velocity, with  $\rho_o$  a reference density for water.  $E_A$  attributable to internal shear of horizontal velocity is parameterized by considering the change in mean horizontal kinetic energy due to complete homogenization of two vertically adjacent layers. We assume that 20% of the change in mean kinetic energy due to the complete homogenization of two layers is available for mixing, whereas the rest is lost to dissipation (Spigel et al. 1986).  $E_R$  is computed as the change in potential energy due to homogenization of two layers, which is positive for gravitationally stable density gradients and negative for unstable density gradients. Where mixing occurs (i.e.,  $E_A > E_R$ ),  $E_A$  is decremented by  $E_R$ . Remaining mixing energy is reduced by dissipation, then transported as a scalar (Spigel et al. 1986).

Computational time-step independence is incorporated into the mixing model by comparing a mixing time-scale,  $T_m$ , with the computational time step,  $\Delta t$ .  $T_m$  can be scaled as the time required for Kelvin–Helmholtz billows to form and decay (Thorpe 1973),

$$T_m = 20 \frac{\Delta U}{g'} \quad (2)$$

where  $\Delta U$  is the horizontal velocity difference between vertically adjacent grid cells. It is assumed that billowing occurs when the gradient Richardson number,

$$\text{Ri} = \frac{N^2}{\left(\frac{\Delta U}{\Delta z}\right)^2} \quad (3)$$

equals a critical value,  $\text{Ri}_c$ . Here,  $\Delta z$  is the vertical distance between vertically adjacent cell centers, and  $N^2$  is the buoyancy frequency discretized as  $g' \Delta z^{-1}$ . Combining Eqs. 2 and 3 gives

$$T_m = \frac{\left(\frac{20}{\text{Ri}_c}\right)}{\left(\frac{\Delta U}{\Delta z}\right)} = \alpha \left|\frac{\Delta U}{\Delta z}\right|^{-1} \quad (4)$$

where  $\alpha = 20\text{Ri}_c^{-1}$  is a constant. Numerical experiments (not shown) indicated that model results are not particularly sensitive to the chosen value of  $\text{Ri}_c$  in Eq. 4 over the range 0.1–2. All numerical results presented in this article used  $\alpha = 50$  corresponding to  $\text{Ri}_c$ , which best reproduced internal wave amplitude and mode, as described in simulations of Lake Kinneret (see “Lake Kinneret”).

Where mixing occurs (i.e.,  $E_A > E_R$ ) and  $\Delta t < T_m$ , complete mixing (homogenization) of two layers should not occur within a single time step. Instead of a complete homogenization of grid cell properties between mixing layers, there is only sufficient time for a partial (or fractional) exchange. A conservative fractional exchange of properties between mixing layers is used to model this partial mixing within a time step. Moreover, the presence of density instabilities during the advection solution can lead to the development of unphysical grid-scale convective circulations, so unstable density gradients are completely mixed regardless of the local value of  $T_m$ . Details of the algorithm employed are given in Laval (2002).

In ELCOM, mixing and advection are calculated separately. Thus, within a computational time step, mixing will not limit the growth of shear until after the advection computation—as it should where  $E_A > E_R$  and the time step is longer than the mixing time scale (i.e.,  $\Delta t > T_m$ ). Therefore, there will be an excess of energy available for mixing in regions where  $E_A > E_R$  and  $\Delta t > T_m$ . Scaling turbulent kinetic energy (TKE) per unit mass as  $0.5U^2$  and dissipation as  $U^3L^{-1}$ , it can be shown that TKE will reduce to less than  $(1 + \alpha)^{-2}$  of its original value within one time step (Tennekes and Lumley 1972). Thus, it can be considered that TKE, in excess of that required to mix a region, will have also decayed within the time step. This can be thought of as the reduced mixing efficiency of highly energetic turbulence (Ivey and Imberger 1991). To capture this in the model, we dissipate the available mixing energy remaining after complete mixing of two layers. Thus, in contrast to Hodges et al. (2000) available mixing energy is only carried over between time steps where no mixing or partial mixing occurs.

By assuming that Kelvin–Helmholtz billows are responsible for turbulent mixing and by using a Richardson number criterion to compute mixing, we are assuming that shear and mixing are collocated. Saggio and Imberger (2001) showed that this is true in Lake Kinneret for vertical scales of less than 10 cm, where  $\text{Ri} < 0.2$ . Typical grid scales used in lake modeling preclude direct simulation of high-frequency (wavelength 10–100 m) waves that can transfer energy to the boundary (Boegman et al. 2003). This flux of energy generated by internal shear from the basin-scale to mixing at the lake boundary is not captured in the present model, nor in any other numerical closure scheme of which the authors are aware.

The effectiveness of the model described in this section

will be demonstrated by its ability to reproduce internal wave and net circulation patterns in Lake Kinneret. These results show quantitative improvement over the previous version of ELCOM (Hodges et al. 2000) in the ability to model internal wave dynamics.

## Lake Kinneret

Lake Kinneret experiences a strong, westerly, daily sea breeze (wind speed  $\sim 10 \text{ m s}^{-1}$ ) during summer afternoons (Assouline and Mahrer 1996). This intense forcing tilts the highly stratified metalimnion, resulting in basin-scale internal waves of various horizontal and vertical modes. The resulting basin-scale internal waves are modified by the earth’s rotation and can be classified as Kelvin and Poincaré waves. In their analysis of thermistor chain data from 1997 and 1998, Antenucci et al. (2000) identified a 24-h period vertical-mode-1 Kelvin wave, a 12-h period vertical-mode-1 Poincaré wave, and 20-h period vertical-modes-2 and -3 Poincaré waves. Hodges et al. (2000) showed that the basic characteristics of the vertical-mode-1, basin-scale Kelvin and Poincaré waves could be simulated using a spatially uniform wind field developed from a single station measurement.

Using drifters, Stocker and Imberger (2003) demonstrated that surface layer vorticity is critical to overall dispersion and transport in Lake Kinneret. However, it is not clear whether surface-layer vorticity calculated from drifter paths is a direct result of wind stress curl or a residual of Kelvin wave circulation, as suggested by Ou and Bennett (1979). Model results presented in this article support the model results of Pan et al. (2002), which show the circulation in Lake Kinneret to be directly forced by surface-layer-averaged wind stress moment.

To demonstrate the mixing model described in the previous section, we compare ELCOM simulations with thermistor chain data for a 12-d period during the summer of 2001. Subsequently, to highlight the importance of wind forcing on simulated basin-scale internal waves and mean circulation, we compare simulations forced with different wind distributions.

*Field data*—Between 19 June 2001 and 1 July 2001 (days 170 and 183 from 1 January), there were six thermistor chain moorings (Fig. 1): four were along the 20-m isobath (Tg, Tf, T9, and T7), one near the lake center (T4), and one southeast of Tf (Ty). Each chain comprised 27 thermistors vertically spaced 0.75 m apart—except in the case of T4, which had 18 thermistors spaced 2.0 m apart. All stations were equipped with wind speed and direction sensors mounted 2.5 m above the water. Station Ty was also equipped with air temperature, relative humidity, and solar radiation sensors. All data were recorded at 10-s intervals, low-pass filtered with a 450-s cut-off, and subsampled at 450 s (corresponding to the ELCOM time step used for all Lake Kinneret simulations). Wind data from shore-based stations were recorded at 600- and 750-s (Tabha and Ein Gev, respectively) intervals. For comparison with other data and for use as ELCOM input, wind data from the two shore-based stations were linearly interpolated to the times of the subsampling used for the wind data from the thermistor chain stations.

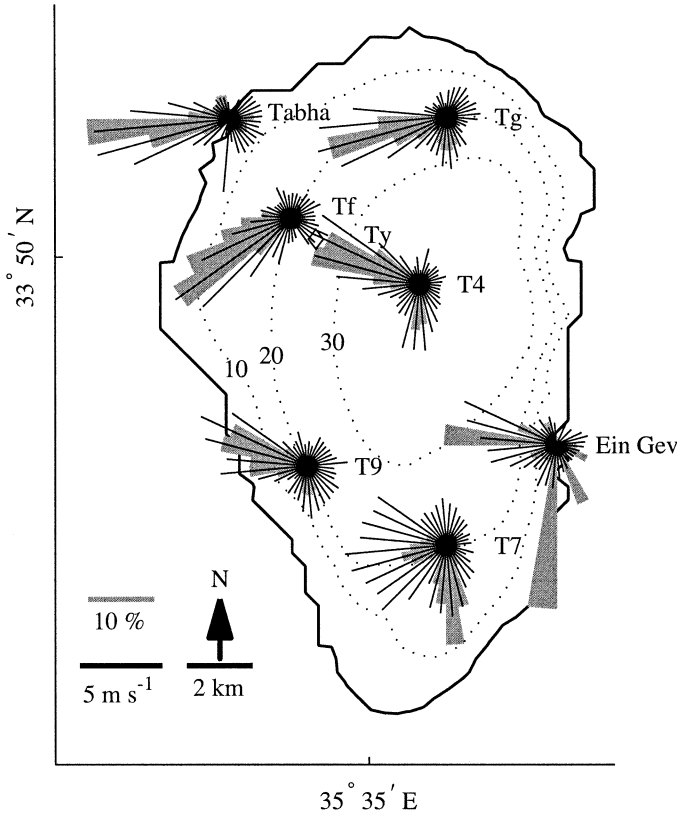


Fig. 1. Lake Kinneret, Israel with 10-, 20-, and 30-m depth contours; wind and thermistor chain stations (Tf, Tg, T4, T7, T9); meteorological station (Ty); and shore wind stations (Tabha and Ein Gev). Average wind speed and frequency of occurrence in 10° direction bins during days 170–183 are plotted as black lines and grey bars, respectively. The wind at Ty is qualitatively similar to Tf. To avoid clutter, wind at Sta. Ty is not shown.

The time-averaged wind field over Lake Kinneret has considerable spatial variation (Fig. 1). The wind in the northwest portion of the lake (Tabha, Tf, Ty, Tg) blows strongest and most often from the western quadrant. The southeast stations (Ein Gev and T7) also have their strongest wind from the western quadrant; however, these sites are more likely to experience southerly winds. Wind speed also tends to weaken from west to east. A time series of horizontally averaged wind stress shows the daily occurrence of the afternoon sea breeze (Fig. 2a). The magnitude of the sea breeze on days 171–174 and 180 is noticeably weaker than on the other days during this period, and there is a secondary peak in the early hours of days 171 and 172, which is associated with an average southerly wind (Fig. 2b). The wind stress on days 171–174 generally has a positive curl (Fig. 2c), with large positive peaks of wind stress curl during the southerly winds on days 171 and 172. During the remaining days, the sea breeze is associated with a strong negative wind stress curl. This description of the wind, calculated from the interpolated wind field, supports the work of Stocker and Imberger (2003). They calculated wind stress curl using cluster analysis applied to the same wind measurements used in the present analysis and found a similar pattern of sea-breeze magnitude and wind curl for this period.

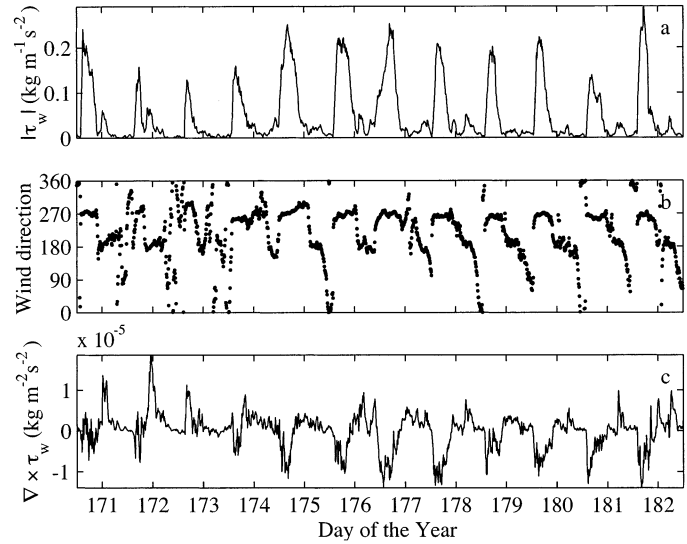


Fig. 2. Record of horizontally averaged wind measurements over Lake Kinneret during 2001: a) wind stress; b) wind direction (meteorological convention); and c) curl of wind stress. Measured wind data were bilinearly interpolated to ELCOM grid, then horizontally averaged.

Using a two-layer approximation to calculate the internal long-wave speed leads to a Burger number of 0.7, which is similar to that computed by Antenucci et al. (2000) for the summer of 1998. At all stations except T4, vertical displacement of isotherms within the metalimnion (Fig. 3) have a pronounced 24-h periodicity associated with a vertical-mode-1 internal Kelvin wave (Antenucci et al. 2000). In the following discussion, only vertical-mode internal waves are considered, and thus, the designation “vertical” will be implied. Tf and T9 display a small peak followed by a large peak within each 24-h period. This is reflected in power spectra of the 23°C isotherm, which show a 24-h peak at all stations (Fig. 4), with Tf and T9 also having pronounced 12-h peaks. Antenucci et al. (2000) observed similar features in a 1998 field experiment at a station near Tf (Sta. T3 in their experiment). They identified the larger peak as a 24-h period Kelvin wave superimposed with the peak of a 12-h Poincaré wave and the smaller peak as a 12-h Poincaré wave superimposed with the trough of the 24-h Kelvin wave. There is an opening of the metalimnion as the smaller peak passes Sta. Tf and T9. A similar feature was identified as mode 2 and 3 Poincaré waves—with a period of about 20 h—by Antenucci et al. (2000). The amplitude of the 24-h periodicity associated with the mode-1 Kelvin wave decays toward the lake center. As a result, the 24-h peak at Sta. T4, near the lake center, is smaller than at the other stations (Fig. 3d).

The 23°C isotherm is near the mid-depth of the metalimnion, and its vertical motion is a good representation of the mode-1 internal wave. The standard deviation of the height of the 23°C isotherm is largest at Tf and T7 and smallest at T4 (Table 1). The 21 and 25°C isotherms are also within the metalimnion, and the standard deviation of their vertical separation is an indication of mode-2 internal wave motions. Note that vertical separation of isotherms will also

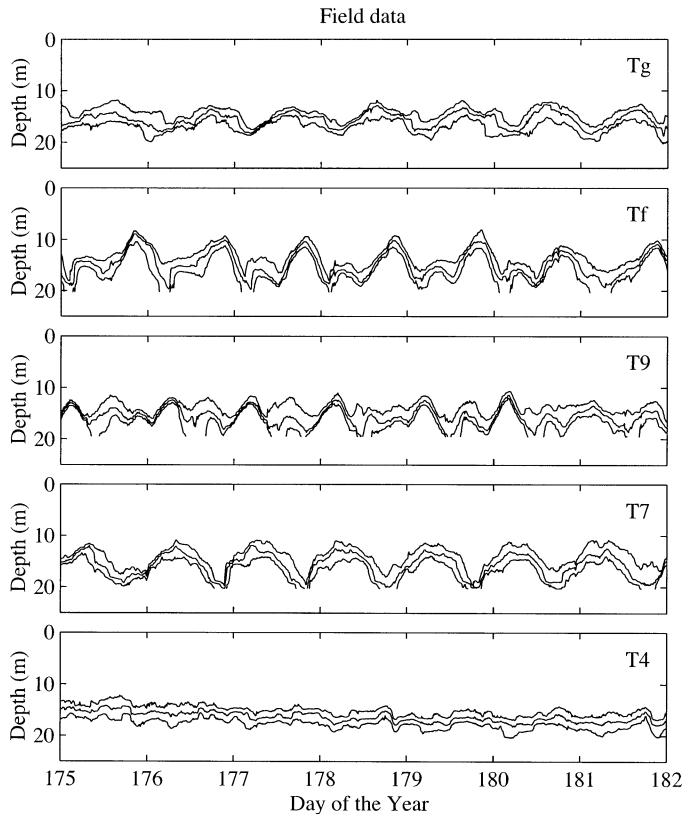


Fig. 3. Record of isotherm displacement in Lake Kinneret during 2001 measured at Stations a) Tg, b) Tf, c) T9, d) T7, and d) T4. In each panel, the top isotherm is 25°C, with a 2°C contour interval. Isotherm heights were determined through linear interpolation. Isotherm heights below the deepest measurement have been excluded.

be influenced by mode-1 waves; however, we will use it primarily as a diagnostic of simulation performance and not to identify high vertical wave modes per se. Vertical separation of 21 and 25°C isotherms at T7 and Tg is about 1 m and is largest at Tf and T9 (Table 2). The phase of the 24-h signal was estimated using Fourier transform (Bendat and Piersol 1986). By comparing the phase of the 24-h signal at Sta. Tf with that of other stations (Table 3), it is possible to follow the Kelvin wave's progression around the lake, starting at Tg, which is about 3 h ahead of Tf, followed by T9 (about 8 h after Tf), and finally at T7, which is almost 11 h out of phase with Tf.

**Simulations**—Simulations were conducted with a model bathymetry having a maximum water depth of 39.5 m, a 400-m horizontal grid size, and a 1-m vertical grid size. Based on atmospheric stability considerations (Rayner 1981), the coefficient of drag for calculating wind stress (i.e.,  $C_D$  in Eq. 1) attains values of  $\sim 2.0 \times 10^{-3}$  during sea-breeze events. Since the daily sea breeze is the dominant wind forcing,  $C_D$  was fixed at  $2.0 \times 10^{-3}$  for all simulations of Lake Kinneret. The density field was initialized with horizontal isotherms taken from a 24-h average of isotherm heights at Sta. T4. This profile was found to lie in the middle of profiles similarly obtained from the other four thermistor chains.

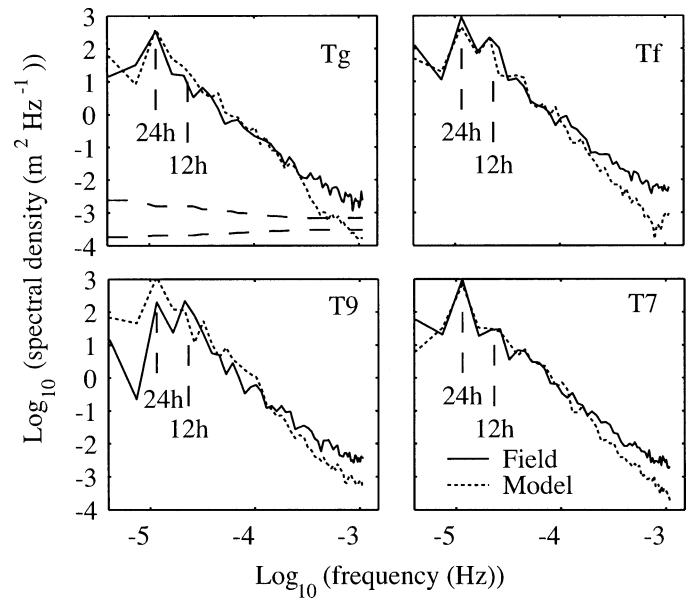


Fig. 4. Power spectra of 23°C isotherm from Lake Kinneret field data and model simulations Run2\_Ty at Stations a) Tg, b) Tf, c) T9, and d) T7. The 95% confidence interval for all panels is given as the vertical distance between the two dashed lines in panel a. Frequency corresponding to 12 and 24 h indicated as dashed vertical lines in all panels.

Simulation spin-up time for the basin-scale internal waves is taken as 24 h (Hodges et al. 2000), the period of the mode-1, internal Kelvin wave. To investigate the importance of wind forcing on simulated basin-scale internal waves and mean surface-layer circulation, we present simulations with three different wind forcings (Table 4): (1) wind data measured at Ty applied over the entire free surface (Run2\_Ty); (2) a spatially varying wind field based on wind data measured at all thermistor chains, Tabha, and Ein Gev (Run2\_VW); and (3) a spatially uniform wind field that has same the horizontally averaged surface shear stress as the spatially varying wind field (Run2\_RMS). The motivation for Run2\_RMS was to compare two simulations with the same horizontally averaged wind stress, where the horizontal average is vectorial (i.e., averaging of components, retaining sign). This approach is similar to that of Findikakis and Law (1999), who temporally averaged the cube of high-frequency wind speed data over the duration of their computational time step in order to calculate net energy input due to wind

Table 1. Standard deviation of the measured and simulated depth of the 23°C isotherm in Lake Kinneret. Values for field data given as height in meters. Values for simulated data are normalized by field value at respective station (i.e., dimensionless).

Station	Field (m)	Run2_Ty	Run2_VW	Run2_RMS
Tg	1.41	1.22	1.39	1.13
Tf	2.56	0.88	0.92	0.75
T9	1.65	1.72	1.05	1.10
T7	2.32	0.99	0.70	0.73
T4	0.95	1.33	1.48	0.91

Table 2. Standard deviation of the measured and simulated difference in depth of the 21 and 25°C isotherms in Lake Kinneret. Values for field data given as height in meters. Values for simulated data are normalized by field value at respective station (i.e., dimensionless).

Station	Field (m)	Run2_Ty	Run2_VW	Run2_RMS
Tg	1.07	1.14	1.30	1.05
Tf	1.21	1.58	1.31	1.02
T9	1.60	2.06	1.37	1.17
T7	1.06	3.42	1.17	1.02
T4	0.63	1.93	1.67	1.49

stirring. The components of wind stress are horizontally averaged, and the wind speed associated with that average wind stress is calculated by inverting Eq. 1 to give

$$\tau_{\text{RMS}} = \frac{(C_D \rho_a)^{-1} \overline{\tau_w}}{\sqrt{(C_D \rho_a)^{-1} |\overline{\tau_w}|}} \quad (5)$$

Here, the overbar denotes an average of components. We define a spatial RMS when the average in Eq. 5 is applied to all estimates of  $\tau_w$  over the lake at a given time and a temporal RMS when that average is applied to estimates of  $\tau_w$  over a particular period of time.

*Uniform wind forcing from Sta. Ty: Run2\_Ty*—As is standard practice in numerical modeling of lakes (e.g., Ahsan and Blumberg 1999), we forced ELCOM with a spatially uniform wind field taken as the measurements at a single point near the lake center: here we use Sta. Ty. Arguably, T4 is closer to the center of the lake; however, we choose Ty in the present work because (1) it has been used in previous modeling studies (e.g., Laval et al. 2003), and (2) it is the station at which the remainder of the meteorological variables used to force ELCOM were measured. The temporal RMS wind properties at this station for the period of interest are summarized in Table 5 and Fig. 1. At this station, both the overall RMS wind and the RMS wind during the sea breeze (identified as the period during which wind speed exceeds the overall RMS) are from west–southwest.

Figure 4 compares displacement spectra of the simulated 23°C isotherm with those attained from field measurements. At all stations but T9 the 12- and 24-h peaks are well reproduced, and the measured and simulated spectra are well matched up to about  $2 \times 10^{-4}$  Hz (1.4 h). The good representation of motions at frequencies higher than that associated with the basin-scale motions (1) shows that the power

Table 3. Phase of the measured and simulated 24-h signal in the 23°C isotherm in Lake Kinneret. All values are given as time difference, in hours, with respect to field data at station Tf. All values are within the 90% coherence confidence interval.

Station	Field (m)	Run2_Ty	Run2_VW	Run2_RMS
Tg	−3.25	−10.71	−4.05	−4.67
Tf	0.00	−2.91	0.76	−2.04
T9	8.22	−2.33	9.56	2.07
T7	11.08	6.28	12.16	10.13

Table 4. Outline of wind forcing for Lake Kinneret simulations.

Simulation		Source
Run2_Ty	Spatially uniform	Derived from station Ty
Run2_VW	Spatially varying	Derived from linear interpolation of all wind stations to model grid
Run2_RMS	Spatially uniform	Derived from spatial RMS (Eq. 5) of wind used in Run2_VW

in the mid-spectrum can be captured even at the coarse grid-scale applied, (2) can be attributed to reduced grid-scale dissipation due to the change in velocity interpolation in the mixing model (see “Numerical method”), and (3) is a qualitative improvement over the simulations of Hodges et al. (2000). Figure 5 shows the simulation results in the same framework as the field data in Fig. 3. Consistent with field observations, isotherm displacements at Sta. T4 are small, whereas at Sta. Tg and T7, isotherm displacements are dominated by a 24-h periodicity. At Sta. Tf and T9 (Fig. 5) there is an interaction of a 24-h with a 12-h oscillation. The simulated wave amplitude is well reproduced, as reflected by the standard deviation of the 23°C isotherm, at all stations but T9, where the wave amplitude is too large (Table 1). Again, consistent with observation, there is a periodic opening of the thermocline at all stations. On closer inspection, it is evident that this periodic opening of the simulated thermocline is exaggerated, especially at Sta. T7 and T9. This is reflected in large values of vertical separation of 21 and 25°C isotherms at all stations (Table 2). The mismatch with observations at Sta. T9 is predominantly due to the large fluctuations in depth of the 21°C isotherm, which rises almost to the free surface during each sea-breeze event. The phase of the simulated 24-h signal is consistently earlier than field observation, ranging from 10 h lead at Sta. T9 to 3 h lead at Sta. Tf (Table 3).

Nondimensional parameters can be used to provide insight into the internal response of a lake to wind forcing. The Wedderburn ( $W$ ) and Lake ( $L_N$ ) numbers (Stevens and Imberger 1996) compare the relative importance of wind stress and basin-scale tilting of isopycnals.  $W$  is defined as

Table 5. Temporal RMS wind, as well as  $W$  and  $L_N$  for Lake Kinneret. “Ty wind” refers to wind measured at station Ty (i.e., Run2\_Ty) and “Varying wind” refers to the spatial RMS wind (i.e., Run2\_VW and Run2\_RMS).  $U$  and  $\Theta$  are the wind speed and direction, respectively. Wind direction uses meteorological convention. The subscript  $SB$  signifies a temporal RMS of sea-breeze wind (defined as wind speed greater than the overall RMS wind speed). Both  $W$  and  $L_N$  were calculated using  $U_{SB}$ .  $W$  uses a surface layer thickness of 12.5 m, and  $L_N$  uses a metalimnion height of 25.5 m.

	Ty wind	Varying wind
$U$ (m s <sup>−1</sup> )	5.6	4.6
$\Theta$	249	257
$U_{SB}$ (m s <sup>−1</sup> )	9.2	7.7
$\Theta_{SB}$	249	265
$L_N$	0.66	0.95
$W$	4.1	5.8

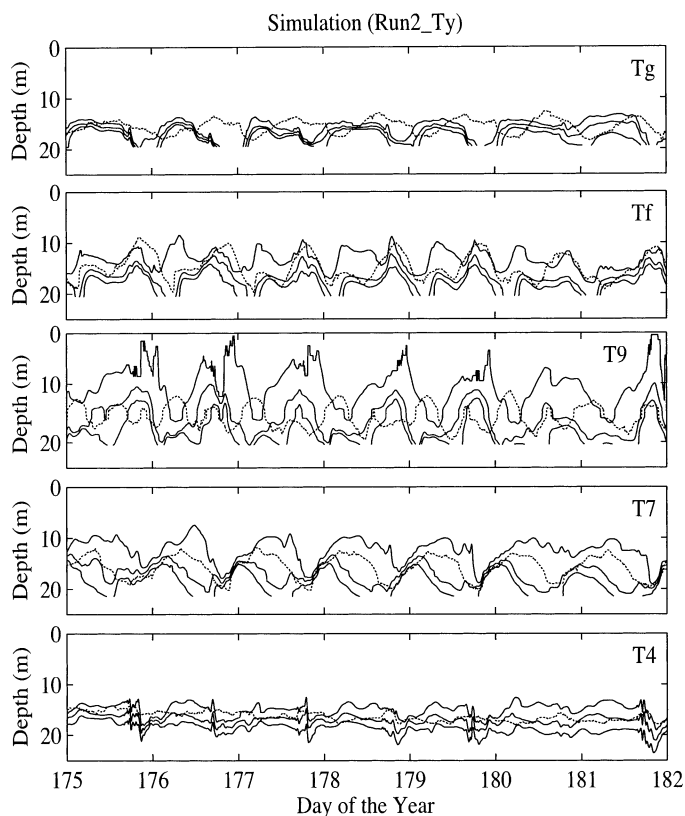


Fig. 5. Simulated (Run2\_Ty) Lake Kinneret isotherms at Stations a) Tg, b) Tf, c) T9, d) T7, and e) T4. In each panel, the top isotherm is 25°C, with a 2°C contour interval. Isotherm heights were determined through linear interpolation. The field measured height of the 23°C isotherm is superimposed (dotted line) for reference. Isotherm heights below the deepest measurement have been excluded.

$$W = \frac{g'h_1^2}{Lu_*^2} \quad (6)$$

where  $h_1$  is the thickness of the surface layer and  $L$  is the along-wind length of the lake at the depth of the base of the surface layer. Here we have used a two-layer approximation to the vertical-mode-1 long internal wave speed.  $L_N$  is defined as

$$L_N = \frac{M_{bc}}{|\tau_w|Az_v} \quad (7)$$

where  $M_{bc}$  is the baroclinic moment about the lake center of volume if the metalimnion were at the point of upwelling,  $A$  is the lake surface area, and  $z_v$  is the depth of the lake center of volume. Both  $W$  and  $L_N$  are steady-state parameters, predicted upwelling of the metalimnion for a sufficiently strong wind event that has a duration of at least  $0.25T_i$ , where  $T_i$  is the fundamental seiche period (Spigel and Imberger 1980).  $W$  has been shown to be related to vertical-mode-2 setup in a three-layer model, whereas  $L_N$  is related to vertical-mode-1 setup (see Imberger and Patterson [1990] for a review). Vertical-mode-1 setup is an overall tilting of the metalimnion, and vertical-mode-2 setup is a downwind thinning and upwind thickening of the metalimnion. Low

values of  $W$  and  $L_N$  (i.e.,  $<1$ ) indicate significant upwelling of metalimnetic water at the free surface.

Although the simulated overall metalimnion tilting (mode 1) is reasonable for the uniform wind case, changes in metalimnion thickness (mode 2) and Kelvin wave phase were not well predicted. Using the temporal RMS of the applied wind speed during sea-breeze events results in  $W = 4.1$  and  $L_N = 0.66$ . Both of these values can be considered small enough that significant mode 1 and 2 setup can be expected to occur. It is clear from the simulation results that mode 1 setup is adequate, but vertical-mode-2 setup is overestimated in the simulations (i.e.,  $W$  is too small). Both  $W$  and  $L_N$  are inversely dependent on the square of the wind speed; hence, overestimating wind forcing in a simulation will result in excessive mode 1 and 2 setup.

*Spatially varying wind forcing: Run2\_VW*—Field data (Fig. 1; Assouline and Mahrer 1996) and numerical simulation data (Avissar and Pan 2000) indicate significant spatial variability in the Lake Kinneret wind field during both sea-breeze and non-sea-breeze periods. A spatially varying field was applied to an ELCOM simulation of Lake Kinneret in Run2\_VW. The difference between this simulation and that forced with a uniform wind field (Run2\_Ty) can be used to infer the effects of spatially varying wind on the internal dynamics. The wind field was constructed from a bilinear interpolation of measured wind data from the eight wind stations to the surface of each numerical water column in ELCOM (i.e., 400-m grid). The spatial interpolation was applied to the wind data at each simulation time step. Snapshots of the interpolated wind field reveal confluence of weak westerlies over most of the lake at midnight (Fig. 6a), with some easterly winds along the eastern shore. Similarly, there is convergence of winds at 0600 h (Fig. 6b); however, by this time there are southerly winds over the southern portion of the lake. At midday (Fig. 6c) there is divergence, with an easterly breeze over most of the lake and a very weak westerly along the eastern shore. By 1800 h (Fig. 6d) the strong-westerly sea breeze dominates over the entire lake. These observations are in general agreement with the atmospheric modeling results of Avissar and Pan (2000) (compare Fig. 6 with their fig. 12), who associate the early morning divergence with a local lake breeze (lake surface warm relative to the surrounding land) combined with katabatic downslope winds from the surrounding topography. The midday divergence of the wind over the lake is attributable to a reversal of the local lake breeze as the surrounding hills heat up. There is an asymmetry to the afternoon lake breeze (preferentially easterly), as the western shore heats up faster than the eastern shore because of the morning sun angle.

Run2\_VW (Fig. 7) shows dramatic improvements over Run2\_Ty (Fig. 5) in the character of the simulated waves at Sta. T9 and T7, with commensurate improvement in wave phase at Tg and little change at Tf. Despite a reduced RMS sea-breeze wind amplitude (Table 5), simulated wave amplitudes at Sta. Tg and Tf are larger than in simulation Run2\_Ty (Table 1). There is considerable reduction in vertical separation of 21 and 25°C isotherms from Run2\_Ty at all stations except Tg. At Sta. T7, the reduction in vertical

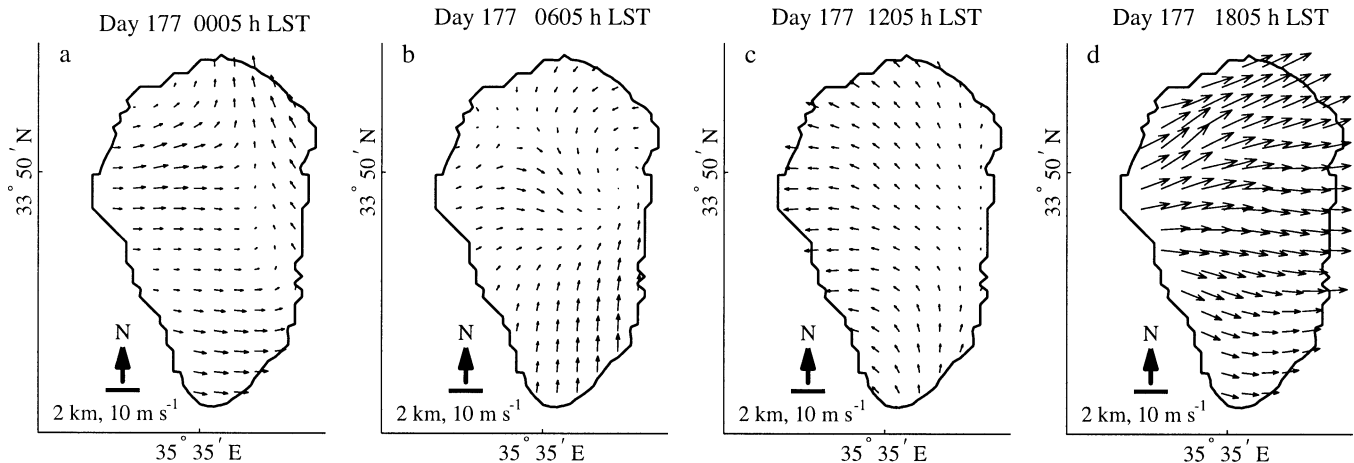


Fig. 6. Snapshots of the spatially interpolated wind field over Lake Kinneret at four different times during day 177. Data were bilinearly interpolated from the eight measurement stations shown in Fig. 1 to the surface of the ELCOM grid. Only every third data point is shown. A comparison of this figure with Fig. 12 of Avissar and Pan (2000) reveals good qualitative agreement.

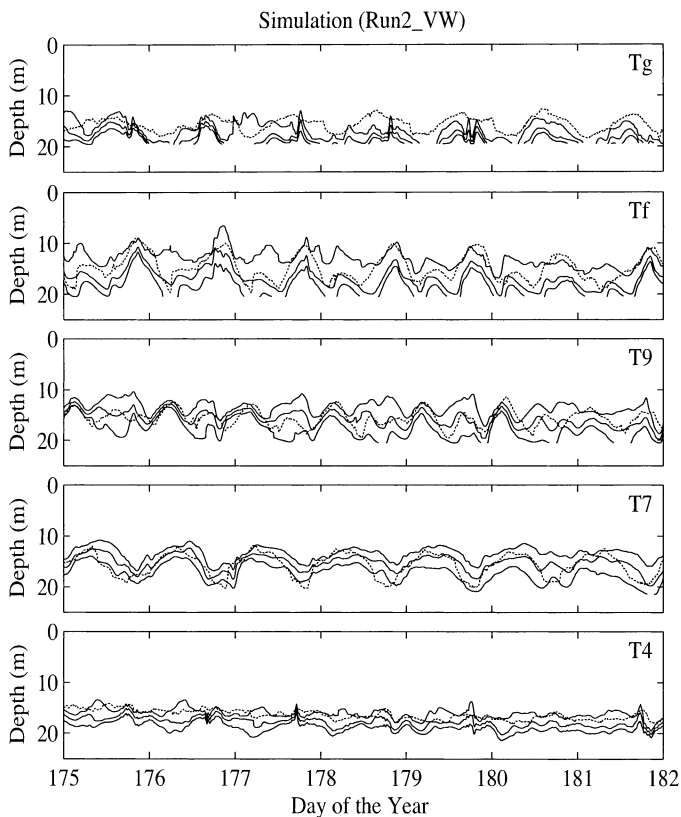


Fig. 7. Simulated (Run\_VW) Lake Kinneret isotherms at Stations a) Tg, b) Tf, c) T9, d) T7, and e) T4. In each panel, the top isotherm is 25°C, with a 2°C contour interval. Isotherm heights were determined through linear interpolation. The field measured height of the 23°C isotherm is superimposed (dotted line) for reference. Isotherm heights below the deepest measurement have been excluded.

separation of 21 and 25°C isotherms is attributable to the reduced mode 2 signal, which results in a contiguous up and down motion of the entire thermocline, with a 24-h period (Fig. 7). This is a closer representation of the observed motion at this station than that simulated in Run2\_Ty (Fig. 5). However, the thermocline compression observed in the wave troughs is no longer well simulated. The simulated isotherm displacements show an improved representation of the phase of the 24-h wave at all stations. This is especially evident in the 21°C isotherm at Sta. Tf and T9, which clearly shows the observed small peak, large peak combination, with the trough separating the two occurring at 1200 h of each day (compare Figs. 3 and 7). Also reproduced is the reduced amplitude of the large peak on day 180 (compare Figs. 3 and 7). The phase of the simulated 24-h signal closely matches field observations, with the largest difference being 1.5 h at T9 (Table 3).

These simulation results give insight into expected model performance when the wind measured at the center of Lake Kinneret (Ty) is used as a basis for a uniform driving wind. The direction of the spatiotemporal RMS of the varying wind field in Run2\_VW is more westerly than that of the temporal RMS of the wind measured at Ty (Table 5). Thus, the metalimnion setup by the spatial RMS wind is along a shorter axis of the lake and is more oblique to the steep eastern side of the lake. Furthermore, the magnitude of the spatiotemporal RMS of the varying wind field in Run2\_VW is less than that of the temporal RMS of the wind measured at Ty (Table 5). As a result,  $W$  and  $L_N$  calculated using the spatially varying wind field are larger than they would be if they had been calculated using wind measured at Sta. Ty. This indicates that both mode 1 and 2 setup should be smaller, which is generally consistent with the simulation results.

*Spatial RMS wind forcing: Run2\_RMS*—To consider the 0th order effect of a spatially varying wind field, an ELCOM simulation of Lake Kinneret was forced with a uniform wind whose magnitude and direction are calculated from the spatial RMS of the interpolated wind field described in the pre-



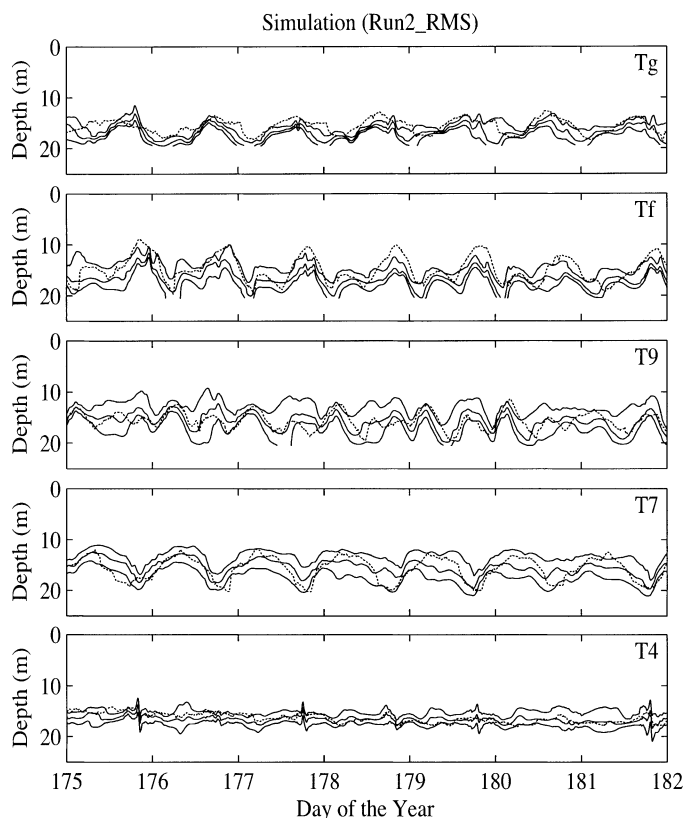


Fig. 8. Simulated (Run2\_RMS) Lake Kinneret isotherms at Stations a) Tg, b) Tf, c) T9, d) T7, and e) T4. In each panel, the top isotherm is 25°C, with a 2°C contour interval. Isotherm heights were determined through linear interpolation. The field measured height of the 23°C isotherm is superimposed (dotted line) for reference. Isotherm heights below the deepest measurement have been excluded.

vious section. Two different wind fields, with the same spatial RMS of velocity and constant drag coefficient (when applied over the same area), will exert the same horizontally averaged shear stress and the same momentum input, resulting in identical  $W$  and  $L_N$ . Thus, a comparison of Run2\_VW and Run2\_RMS shows the effect of spatial variation in wind direction without the distortion of momentum input that occurs when wind speed from a single station is used as a model boundary condition. The overall results are similar and in some instances better (Sta. Tg) than those of the simulation forced with a spatially varying wind (Tables 1–3; Fig. 8). The improvements in the simulated wave character at Sta. T9 and T7 due to applying a spatially varying wind field (see previous section) are retained in this simulation. As well, there is less deepening of the metalimnion at Sta. Tg, and the waves are now extremely well reproduced (Fig. 8), and even small details, such as the thermocline expansions, occurring at 0000 h on days 179 and 180 are well simulated. Degradation of the wind field from spatially varying to uniform should have resulted in a commensurate degradation of results; however, we observe the converse. The improvement of internal wave representation at Sta. Tg (due to reduced metalimnetic deepening) indicates that the poor wind data coverage in the northeastern portion of the lake

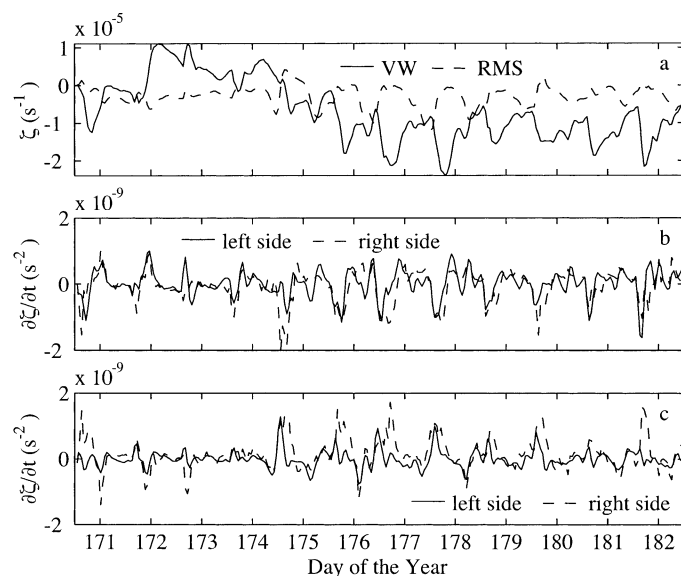


Fig. 9. A time series of vorticity and a balance of the left and right sides of Eq. 12: a) horizontally averaged vorticity of horizontal, surface-layer velocity for simulations Run2\_VW and Run2\_RMS; and comparisons of the left and right sides of Eq. 12 for simulations b) Run2\_VW and c) Run2\_RMS.

(Fig. 1) resulted in an error in the interpolated wind field that is locally significant and that the error associated with assuming a uniform wind field is smaller. Overall, the waves simulated using a spatial RMS wind best reproduce the field observations, indicating that, to first order, the most important characteristic of the wind field over Lake Kinneret for producing the observed internal waves is the horizontally averaged wind shear stress. However, as is described in the following section, the curl of the wind field is an essential component of the mean surface-layer vorticity balance in Lake Kinneret.

*Mean surface-layer circulation*—Mean surface-layer circulation is quantified as the horizontally averaged surface-layer vorticity, where surface layer is taken to be water warmer than 21°C and where vorticity is the curl of the depth-averaged, surface-layer, horizontal velocity. During days 172–174, horizontally averaged surface-layer vorticity in Run2\_VW is positive, whereas it remains close to zero in Run2\_RMS (Fig. 9a). After day 174, horizontally averaged surface-layer vorticity in Run2\_VW becomes negative, decreasing during each sea breeze and increasing as the sea breeze dies down (Fig. 9a). This is contrary to Run2\_RMS, in which after day 174, horizontally averaged surface-layer vorticity begins fluctuating diurnally, increasing with each sea breeze and decreasing as the sea breeze dies down (Fig. 9a). The following discussion uses a layer-averaged vorticity balance to explain the difference in vorticity between these two simulations.

Neglecting advection of vorticity, the shallow-water, layer-averaged vorticity equation may be written as

$$\frac{\partial \zeta}{\partial t} = -(f + \zeta) \nabla \cdot \mathbf{u} + \nabla \times \left( \frac{\boldsymbol{\tau}_w}{\rho_o H} \right) - \nabla \times \left( \frac{\boldsymbol{\tau}_b}{\rho_o H} \right) \quad (8)$$

Here,  $\zeta = \nabla \times \mathbf{u}$  is the vorticity of the vertically layer-averaged, horizontal velocity  $\mathbf{u}$ ,  $\tau_w$  is defined in Eq. 1,  $\tau_b$  is bottom stress, and  $H$  is the layer thickness. The latitude at Lake Kinneret is  $33.5^\circ\text{N}$ , which results in  $f = 8 \times 10^{-5} \text{ s}^{-1}$ . The first term on the right side of Eq. 8 represents a change in vorticity as a result of vortex stretching. Using the vertically layer-averaged continuity equation, it can be shown that

$$-(f + \zeta)\nabla \cdot \mathbf{u} = \frac{(f + \zeta)}{H} \left( \frac{\partial H}{\partial t} + \mathbf{u} \cdot \nabla H \right) \quad (9)$$

For the time scales considered here (i.e.,  $\sim 10$  d), the time rate of change of the horizontally averaged layer thickness is negligible (i.e.,  $\partial H/\partial t \sim 0$ ), and vortex stretching is predominantly due to advection along variations in layer thickness. The overall vorticity input by wind stress (combined wind stress moment) can be expanded using the following vector identity:

$$\nabla \times \left( \frac{\tau_w}{\rho_o H} \right) = \underbrace{\left( \frac{1}{\rho_o H} \right)}_{\text{combined wind stress moment}} \nabla \times \tau_w + \underbrace{\left( \frac{\tau_w}{\rho_o H^2} \right)}_{\text{topological moment}} \times \nabla H \quad (10)$$

wind stress curl
bottom stress curl

Equation 10 implies that wind stress applied over a layer of water of varying thickness can introduce vorticity through (1) wind stress curl and (2) a topological moment that is attributable to variations in layer thickness in a direction perpendicular to the wind stress. Thus, by the latter mechanism, surface-layer vorticity may be induced by a uniform wind stress. As a result of uncertainties in calculating bottom stress (discussed below), we will not consider an expansion of the bottom stress term in Eq. 8. Physically, the bottom stress term represents a flux of vorticity from the surface layer to the lake bottom in shallow water and to the underlying metalimnion in deeper water. The flux of vorticity to the lake bottom is poorly simulated in ELCOM because the lake bottom is discretized with a z-coordinate computational grid. Despite the use of free-slip bottom boundary conditions, the stair-step nature of the discretized bottom topography results in a loss of momentum, the rate of which is grid-size dependent (Adcroft and Marshall 1998). For this reason, bottom stress is parameterized using a simple linear relation

$$\tau_b = \rho_o K \mathbf{u} \quad (11)$$

with  $K$  a dimensional bottom-drag coefficient.

Applying Eqs. 9 and 10 to Eq. 8 leads to

$$\begin{aligned} \frac{\partial \zeta}{\partial t} = & \underbrace{\frac{(f + \zeta)}{H} \mathbf{u} \cdot \nabla H}_{\text{stretching}} + \underbrace{\left( \frac{1}{\rho_o H} \right) \nabla \times \tau_w}_{\text{wind stress curl}} + \underbrace{\left( \frac{\tau_w}{\rho_o H^2} \right) \times \nabla H}_{\text{topological moment}} \\ & - \underbrace{\nabla \times \left( \frac{\tau_b}{\rho_o H} \right)}_{\text{bottom stress moment}} \end{aligned} \quad (12)$$

Thus, the time rate of change of layer-averaged vorticity is

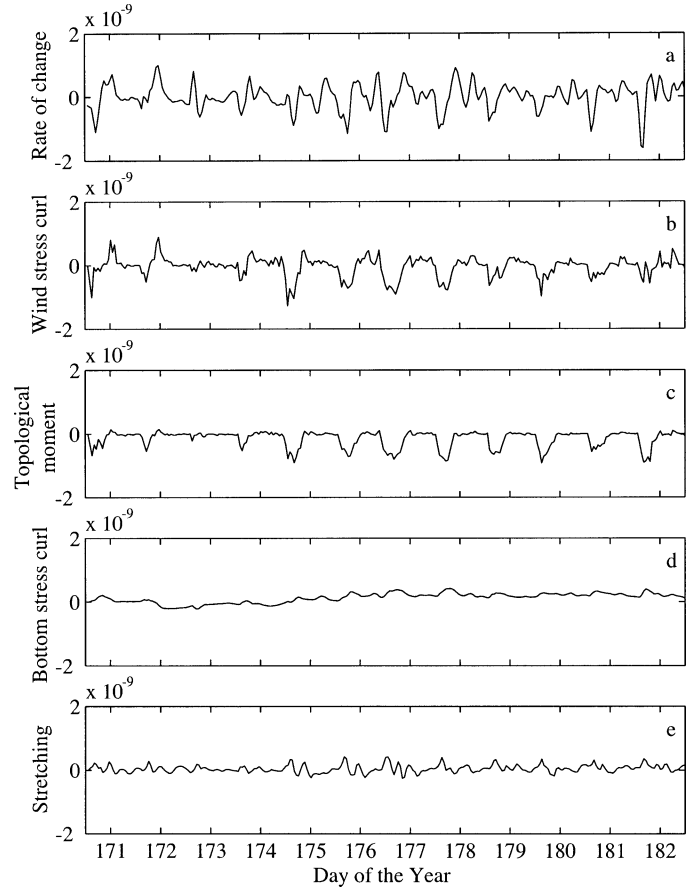


Fig. 10. Surface-layer vorticity balance in Lake Kinneret for simulation Run2\_VW, presented as a comparison of each term in Eq. 12. The units of the ordinate of each panel appear in  $\text{s}^{-2}$ .

due to the sum of vortex stretching, wind stress curl, topological moment, and bottom stress moment. Using  $K = 2 \times 10^{-4} \text{ m s}^{-1}$  leads to a good comparison between the horizontally averaged time rate of change of surface-layer vorticity and the sum of the horizontal average of the four terms on the right side of Eq. 12 for both Run2\_VW (Fig. 9b) and Run2\_RMS (Fig. 9c), when water shallower than 5 m is excluded from the horizontal average for Run2\_VW. Including water shallower than 5 m in the horizontal average for Run2\_VW results in a poor comparison, which is likely due to a breakdown of the linear bottom-drag formulation in shallow regions, where there are large accelerations due to large values of the wind momentum source term  $u_*^2 H^{-1}$ . Such accelerations are especially large along the northern shore, where the highest sea-breeze velocities occur. In Run2\_RMS, however, regions shallower than 5 m must be included in the horizontal average. Otherwise, the sum of the terms on the right side of Eq. 12 is too small to balance the left side. This implies that in Run2\_RMS, vorticity is generated in the shallow regions and advected to the deeper regions of the lake, whereas in Run2\_VW, this mechanism is of secondary importance.

The main difference between Run2\_VW and Run2\_RMS is that wind stress curl is a significant source of vorticity in Run2\_VW (Fig. 10b), whereas in Run2\_RMS, it is exactly

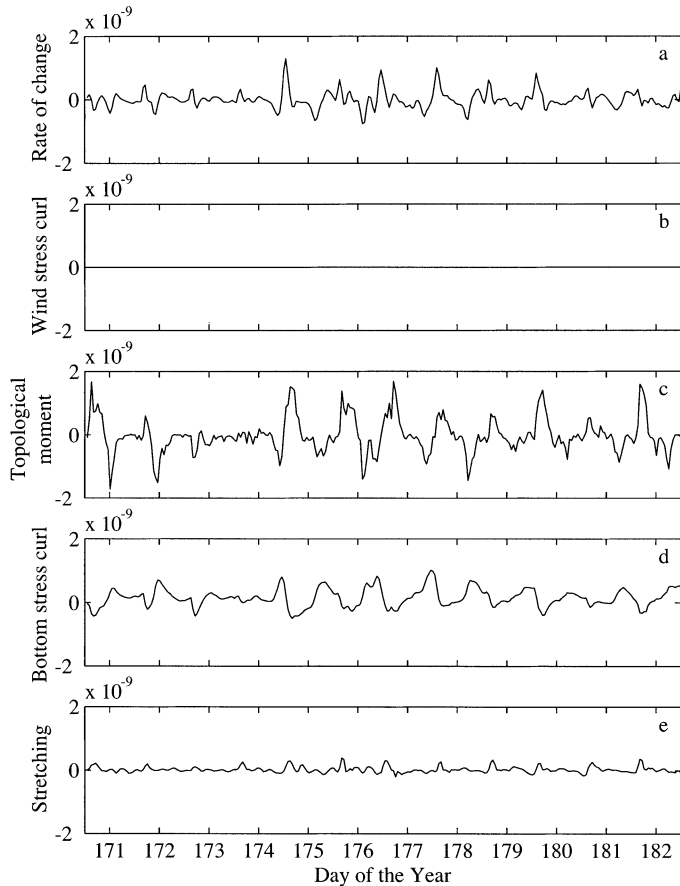


Fig. 11. Surface-layer vorticity balance in Lake Kinneret for simulation Run2\_RMS, presented as a comparison of each term in Eq. 12. The units of the ordinate of each panel appear in  $s^{-2}$ .

zero (Fig. 11b). Figure 10 compares the horizontal average of each of the terms in Eq. 12 for Run2\_VW. The wind stress curl (Fig. 10b) and topological moment (Fig. 10c) are of similar value and together contribute a large negative vorticity input from day 174 onward. Bottom stress moment (Fig. 10d) provides a small amount of vorticity counter to the mean circulation that develops after day 175, whereas vortex stretching (Fig. 10e) contributes little to the overall vorticity balance. Vorticity in Run2\_RMS is predominantly generated by the topological moment (Fig. 11c) and dissipated by bottom friction (Fig. 11d), with vortex stretching (Fig. 11e) playing a relatively minor role. In Run2\_RMS, the net balance of the terms on the right side of Eq. 12 results in an increase in surface-layer vorticity during the sea breeze and a slow decrease between sea breezes. Although the topological moment in Run2\_VW is negative during the sea breeze (Fig. 10c), the topological moment in Run2\_RMS is positive during the sea breeze (Fig. 11c).

The mean circulation in both simulations is attributable to a balance between wind forcing and bottom friction. In Run2\_VW, the vorticity contributed by wind forcing is predominantly negative during the sea breeze and only weakly positive between sea breezes, so vorticity oscillates diurnally about a negative mean value. In contrast, for Run2\_RMS, the wind forcing contributes positive vorticity during sea

breezes and negative vorticity between sea breezes, resulting in vorticity that oscillates diurnally about a mean value close to zero. Thus, during the sea breeze, it is the difference in sign of the combined wind-forcing terms that results in mean surface-layer vorticity decreasing in Run2\_VW and increasing in Run2\_RMS.

These results extend the work of Pan et al. (2002), who showed that the depth-averaged vorticity in Lake Kinneret during a sea-breeze event could be accounted for by equating the time rate of change of surface-layer vorticity with the sum of the wind stress curl and topological moment. They predicted circulation with a positive, horizontally averaged vorticity, corresponding to the horizontally averaged positive curl of the sea-breeze wind stress. This supports our result that the overall lake vorticity is determined by the horizontally averaged curl of wind stress.

## Conclusions

Basin-scale internal wave motion during summer in Lake Kinneret is well simulated with a uniform wind field, provided that the horizontally averaged wind stress is well represented. Using a spatially uniform wind field acquired from measurements at a single station (Run2\_Ty) was found to well reproduce observed isotherm displacements. However, the simulated amplitude of vertical-mode-2 internal waves tended to be too large, and the phase error of the vertical-mode-1, 24-h Kelvin ranged from 3 to 10 h. Applying a uniform wind field derived from the horizontally averaged wind stress (Run2\_RMS) improved the overall wave character. Thus, even though Lake Kinneret has a simple bathymetry, high topography to the east and west of the lake results in spatial variations in wind that are important in determining the amplitude and phase of the various modes and types of internal waves. Simulation results could be improved further by a more accurate representation of the wind spatial distribution, particularly along the eastern shore, where in this study there was little wind data coverage. Further improvements may be realized through the consideration of spatial variability of the coefficient of drag ( $C_D$ ) used for calculating wind shear as well as spatial variability of surface heat fluxes.

In Lake Kinneret, mean surface-layer circulation is shown to be directly driven by wind stress curl and topological moment, and hence, the horizontal distribution of wind stress is important. For this case, the wind stress curl and topological moment are of similar magnitude and of the same sign. As well, the wind stress curl and wind direction with respect to the bottom topography for Lake Kinneret makes the sign of the wind stress curl and topological moment the same; however, for different lake bathymetries or wind fields, these two terms could be of opposite sign.

The overall picture that emerges from Lake Kinneret is a setup of the metalimnion by the daily sea breeze and subsequent internal-wave motions. These internal-wave motions can be well modeled using a uniform wind field, provided that this wind field represents the horizontally averaged wind stress (i.e., spatial RMS). In contrast, mean surface-layer circulation is predominantly directly forced by the combined

wind stress moment, and hence, a spatially varying wind field is required to simulate the surface-layer circulation.

## References

- ADCROFT, A., AND D. MARSHALL. 1998. How slippery are piecewise-constant coastlines in numerical models? *Tellus* **50A**: 95–108.
- AHSAN, A.K.M.Q., AND A. F. BLUMBERG. 1999. Three-dimensional hydrothermal model of Onondaga Lake, New York. *J. Hydraulic Eng.* **125**: 912–923.
- ANTENUCCI, J. P., J. IMBERGER, AND A. SAGGIO. 2000. Seasonal evolution of the basin-scale internal wave field in a large stratified lake. *Limnol. Oceanogr.* **45**: 1621–1638.
- ASSOULINE, S., AND Y. MAHRER. 1996. Spatial and temporal variability in microclimate and evaporation over Lake Kinneret: Experimental evaluation. *J. Appl. Meteorol.* **35**: 1076–1084.
- AVISSAR, R., AND H. PAN. 2000. Simulations of the summer hydro-meteorological processes of Lake Kinneret. *J. Appl. Hydro-meteorol.* **1**: 95–109.
- BENDAT, J., AND A. PERSOL. 1986. *Random data: Analysis and measurement procedures*, 2nd ed. Wiley.
- BOEGMAN, L., J. IMBERGER, G. N. IVEY, AND J. P. ANTENUCCI. 2003. High-frequency internal waves in large stratified lakes. *Limnol. Oceanogr.* **48**: 895–919.
- CASULLI, V., AND E. CATTANI. 1994. Stability, accuracy and efficiency of a semi-implicit method for three dimensional shallow water flow. *Computers Math. Applications.* **27**: 99–112.
- , AND R. T. CHENG. 1992. Semi-implicit finite difference methods for three-dimensional shallow water flow. *Int. J. Numerical Methods Fluids.* **15**: 629–648.
- DIETRICH, D. E. 1997. Application of a modified Arakawa 'A' grid ocean model having reduced numerical dispersion to the Gulf of Mexico circulation. *Dynamics Atmos. Oceans.* **27**: 201–217.
- FINDIKAKIS, A. N., AND A. W. K. LAW. 1999. Wind mixing in temperature simulations for lakes and reservoirs. *J. Environ. Eng.* **125**: 420–428.
- HODGES, B. R. 2000. *Numerical techniques in CWR-ELCOM*. Technical report, Centre for Water Research, University of Western Australia, Nedlands, Western Australia, 6907. Reference WP 1422-BH.
- , J. IMBERGER, A. SAGGIO, AND K. WINTERS. 2000. Modeling basin-scale internal waves in a stratified lake. *Limnol. Oceanogr.* **45**: 1603–1620.
- IMBERGER, J. 1998. Flux paths in a stratified lake: A review, p. 1–17. *In* J. Imberger [ed.], *Physical Processes in Lakes and Oceans*. American Geophysical Union.
- , AND J. C. PATTERSON. 1990. Physical limnology. *Adv. Appl. Mech.* **27**: 303–475.
- IVEY, G. N., AND J. IMBERGER. 1991. On the nature of turbulence in a stratified fluid, part I: The energetics of mixing. *J. Phys. Oceanogr.* **21**: 650–658.
- KRAUS, E. B., AND J. S. TURNER. 1967. A one-dimensional model of the seasonal thermocline: II. The general theory and its consequences. *Tellus* **19**: 98–105.
- LAVAL, B. 2002. *Modelling transport in lakes and estuaries*. Ph.D. thesis. University of Western Australia.
- , B. R. HODGES, AND J. IMBERGER. 2003. Numerical diffusion in 3D, hydrostatic, z-level lake models. *J. Hydraulic Eng.* **129**: 215–224.
- LEONARD, B. P. 1991. The ULTIMATE conservative difference scheme applied to unsteady one-dimensional advection. *Comp. Methods Appl. Mech. Eng.* **88**: 17–74.
- OU, H. W., AND J. R. BENNETT. 1979. A theory of the mean flow driven by long internal waves in a rotating basin, with application to Lake Kinneret. *J. Phys. Oceanogr.* **9**: 1112–1125.
- PAN, H., R. AVISSAR, AND D. B. HAIDVOGEL. 2002. Summer circulation and temperature structure of Lake Kinneret. *J. Phys. Oceanogr.* **32**: 295–313.
- RAYNER, K. N. 1981. *Diurnal energetics of a reservoir surface layer*. Technical report, Centre for Water Research, Department of Environmental Engineering, University of Western Australia, Crawly, Western Australia, CWR report number: ED-80-005.
- SAGGIO, A., AND J. IMBERGER. 2001. Mixing and turbulent fluxes in the metalimnion of a stratified lake. *Limnol. Oceanogr.* **46**: 392–409.
- SPIGEL, R. H., AND J. IMBERGER. 1980. The classification of mixed-layer dynamics in lakes of small to medium size. *J. Phys. Oceanogr.* **10**: 1104–1121.
- , ———, AND K. N. RAYNER. 1986. Modeling the diurnal mixed layer. *Limnol. Oceanogr.* **31**: 533–556.
- STANFORTH, A., AND J. CÔTÉ. 1991. Semi-Lagrangian integration schemes for atmospheric models—a review. *Monthly Weather Rev.* **119**: 2206–2223.
- STEVENS, C., AND J. IMBERGER. 1996. The initial response of a stratified lake to a surface shear stress. *J. Fluid Mech.* **312**: 39–66.
- STOCKER, R., AND J. IMBERGER. 2003. Horizontal dispersion in the surface layer of a stratified lake. *Limnol. Oceanogr.* **48**: 971–982.
- STRUB, P. T., AND T. M. POWELL. 1986. Wind-driven surface transport in stratified closed basins: Direct versus residual circulations. *J. Geophys. Res.* **91**: 8497–8508.
- TENNEKES, H., AND J. LUMLEY. 1972. *A first course in turbulence*. MIT Press.
- THORPE, S. A. 1973. Turbulence in stably stratified fluids: A review of laboratory experiments. *Boundary-Layer Meteorol.* **5**: 95–119.

Received: 21 March 2002  
Accepted: 9 December 2002  
Amended: 18 January 2003